Nano Research

Open Access

Research Article

Bipolar polymer-graphene composite cathodes for high-performance aqueous zinc-ion batteries with efficient self-charging capability

Yongqi Mi[1], Shaopei Yang[1], Shimeng Guo[1], Jiajun He[1], Yujia Guo[1], Yanxuan Yin[2], and Pengcheng Du[1] ✉

[1] *State Key Laboratory of Natural Product Chemistry, Institute of Polymer Science and Engineering, College of Chemistry and Chemical Engineering, Lanzhou University, Lanzhou 730000, China*
[2] *Cuiying Honors College, Lanzhou University, Lanzhou 730000, China*

Cite this article: *Nano Research*, **2026**, *19*, 94908674. https://doi.org/10.26599/NR.2026.94908674

ABSTRACT: Developing organic cathodes that combine robust electrochemical performance with functional versatility is pivotal for the advancement of aqueous zinc-ion batteries (ZIBs). Herein, we design a bipolar polymer-graphene composite cathode, poly(1,8-diaminonaphthalene)-reduced graphene oxide (PDAN-rGO), through *in situ* polymerization on graphene sheets. The conductive graphene network and bipolar redox-active polymer synergistically enable a dual-ion storage mechanism involving both Zn^{2+} and $CF_3SO_3^-$. The PDAN-rGO cathode delivers a high reversible capacity of 162.67 mAh·g^{-1} at 0.1 A·g^{-1}, excellent rate performance (101.12 mAh·g^{-1} at 20 A·g^{-1}), and outstanding cycling stability with 89.18% capacity retention after 10,000 cycles. Notably, the cathode exhibits a thermodynamically favorable redox potential that allows spontaneous chemical oxidation by atmospheric oxygen, leading to an efficient self-charging function. The battery achieves an open-circuit voltage of 1.25 V and recovers 95.2% of its capacity without any external power input. This work offers a high-performance bipolar cathode design and a feasible strategy for building self-sustaining energy storage systems.

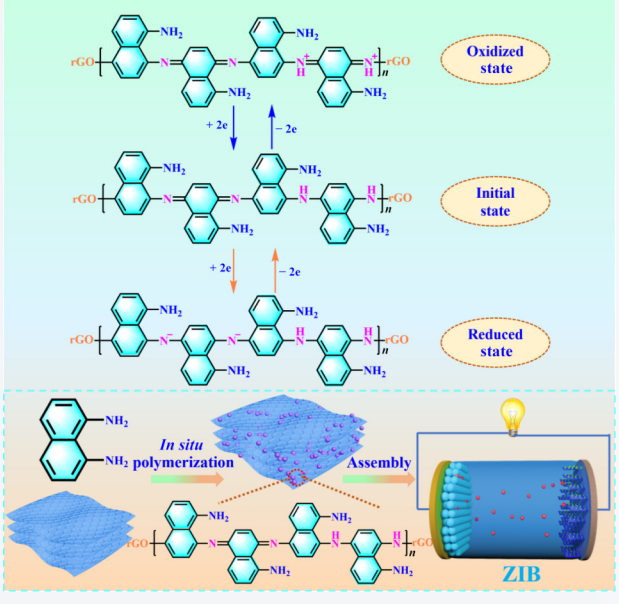

KEYWORDS: bipolar polymer, graphene-based composite electrode, aqueous zinc-ion battery, self-charging

1 Introduction

The growing global energy demand and increasing environmental concerns have intensified the need for clean and sustainable energy storage technologies [1, 2]. To accelerate the adoption of clean energy, electrochemical energy storage devices have garnered significant attention and exhibit considerable potential [3]. A multitude of secondary batteries have been developed, including lithium-ion batteries (LIBs), sodium-ion batteries (SIBs), zinc-ion batteries (ZIBs), and so on [4–7]. LIBs have an extremely high energy density and are one of the most mature technologies in the energy storage field at present, which have been applied in the commercial field [8]. Nonetheless, the concerning safety profile of organic LIBs and the scarcity of lithium resources have significantly impeded their advancement in the energy storage domain [9]. Consequently, to circumvent the limitations of the aforementioned LIBs, a proliferation of safe and reliable aqueous batteries has emerged, generating considerable research interest [10].

Aqueous ZIBs demonstrate several advantages, including a high theoretical capacity (820 mAh·g^{-1} and 5855 mAh·cm^{-3}), a low redox potential (−0.763 V vs. standard hydrogen electrode (SHE)), enhanced safety, intrinsic safety, and natural abundance [11]. These characteristics make them strong candidates for next-generation energy storage systems. Recently, various inorganic cathode materials, such as MnO_2, V_2O_5, vanadium-based derivatives, and Prussian blue analogs, have been explored as ZIB cathodes [12–15]. However, the continuous insertion and extraction of Zn^{2+} ions during the charge/discharge process can lead to structural collapse,

Received: January 4, 2026; **Revised:** March 5, 2026
Accepted: March 25, 2026

✉Address correspondence to dupch@lzu.edu.cn

causing reduced specific capacity and cycling stability [16, 17]. Furthermore, the synthesis of inorganic materials with complex structures is often inefficient, and their potential toxicity challenges their long-term sustainability and commercialization [15, 18–20]. In contrast, organic electrode materials have garnered considerable attention due to their environmentally friendly, sustainable, and cost-effective nature, providing a greener alternative to traditional metal-based electrodes. Organic compounds, including conjugated polymers and small organic molecules, often exhibit high theoretical capacities owing to their multi-electron transfer capability during charge/discharge cycles [21, 22]. However, the application of organic materials is hindered by their relatively low electrical conductivity, which limits power density and overall performance, as well as by their susceptibility to capacity degradation and structural instability during prolonged cycling [23–28]. To address these limitations, researchers have focused on developing composite electrodes by integrating highly conductive materials, such as graphene, activated carbon (AC), and MXene [29–31]. These composite materials provide additional active sites for embedding organic polymers, mitigate volume expansion during cycling, and enhance overall electrochemical performance. By combining the advantages of both organic and conductive materials, composite electrodes achieve high specific capacity, excellent rate capability, and superior long-term cycling stability.

In addition, a large amount of O_2 exists in the air, and its ability to participate in various redox reactions has attracted much attention in the field of energy storage [23, 30, 32]. Therefore, combining the chemical energy of oxygen with the electrical energy in the electrode material is an extremely efficient energy storage method [33]. Crucially, a discharged polymer cathode (electrochemically reduced in aqueous electrolyte) can be spontaneously re-oxidized directly by ambient air. This air-driven oxidation effectively mirrors the electrochemical charging process, enabling the development of self-charging aqueous ZIBs. Such air-rechargeable systems hold significant promise for large-scale sustainable power generation. For instance, Wang and co-workers demonstrated a self-charging ZIB using 1,5-naphthalenediamine-derived polymer, which reaches a charged state upon air exposure [23]. Recently, several organic electrodes have been developed as cathodes for self-charged ZIBs. These all prove the feasibility of self-charging ZIBs. Therefore, the cathode materials play a crucial role in the self-charging performance of self-charging ZIBs. So far, the self-charging properties of some organic cathodes have been reported, such as poly(1,5-naphthalenediamine) (poly(1,5-NAPD)), poly(4-hydroxy-diphenylamine) (HDPA), and benzo[*i*]benzo[6,7]quinoxalino[2,3-*a*]benzo[6,7]quinoxalino [2,3-*c*]phenazine-5,8,13,16,21,24-hexaone (BQPH) [23, 34, 35]. For poly(1,5-NAPD), BQPH, and HDPA, they require about 12 h to achieve the fully charged state by air oxidation [23, 34, 35]. However, the amino-containing polymers, such as polyaniline (PANI), generally showed low discharge median voltage at ~ 0.7 V. For a practical self-charging ZIBs, the high voltage plateau, high areal capacity, and less self-charging time of the cathode are critical issues to evaluate the power capability. Su et al. blended PANI with Pt/C catalyst to accelerate the self-charging rate, making the composite cathode fully air-charged in 12 h [36]. Without Pt/C, the discharged PANI cathode can only reach half-charged state even exposed to air for a few days. Li et al. reported poly(4,4́-diaminodiphenylamine) coated on AC can be fully air-charged in 3 h, reaching an open circuit voltage of 1.2 V [30]. Xu et al. developed HDPA onto mesoporous activated carbon and showed a relatively high discharge voltage plateau at ~ 1.1 V [34]. Thus, it remains a challenge to develop organic cathode materials that combine high discharge voltage, rapid self-charging, and high capacity.

Herein, we report a bipolar-type polymer-graphene composite (poly(1,8-diaminonaphthalene)-reduced graphene oxide (PDAN-rGO)), synthesized via *in situ* polymerization of 1,8-diaminonaphthalene (1,8-DAN) on graphene oxide, followed by solvothermal reduction. The composite serves as a high-performance cathode for aqueous ZIBs, delivering high capacity (162.67 mAh·g^{-1} at 0.1 A·g^{-1}), exceptional rate performance, and long-term cyclability (89.18% of its initial capacity after 10,000 cycles). More importantly, the material exhibits efficient self-charging behavior upon air exposure, achieving an open-circuit voltage (OCV) of 1.25 V and a high cumulative discharge capacity of 2216.6 mAh·g^{-1}. This work provides a feasible strategy toward high-voltage, fast self-charging ZIBs using rationally designed polymer-graphene composites.

2 Experimental

2.1 Materials

1,8-DAN, zinc trifluoro-methanesulfonate ($Zn(CF_3SO_3)_2$), and ammonium persulfate (APS) were purchased from Shanghai Aladdin Biochemical Technology Co., Ltd. Polyvinylidene fluoride (PVDF, HSC 900) was supplied by Arkema. Polytetrafluoroethylene (PTFE) emulsion (D210C, 60 wt.% dispersion in H_2O) was obtained from Daikin Industries. Zn foil (99.995%, 100 μm) was obtained from Wuhan Luojia Yanxin Technology Co., Ltd. Glass fiber was obtained from Shanghai Jieyi Biotechnology Co., Ltd. N,N-Dimethylformamide (DMF) was used as received from Tianjin Lianlong Chemical Co., Ltd. GO was synthesized via a modified Hummers method. All experiments were performed using deionized (DI) water and analytical-grade chemical reagents without further purification.

2.2 Preparation of graphene-PDAN composite (PDAN-rGO)

Composites with different mass ratios of 1,8-DAN to GO (denoted as PDAN-rGO-*x*, where x = 1–7) were synthesized by *in situ* oxidative polymerization of 1,8-DAN in the presence of GO, followed by solvothermal reduction. In a typical procedure, 0.02 g of GO was dispersed in 40 mL of DMF by bath sonication to form a homogeneous suspension. Under vigorous stirring, 0.1 g of 1,8-DAN was added to the mixture. Then, 50 mL of an aqueous HCl solution containing 0.25 g of APS was added dropwise while maintaining the temperature below 0 °C. After stirring for 12 h, the resulting suspension was transferred into a 100 mL Teflon-lined autoclave and heated at 180 °C for 12 h. The product was collected by centrifugation after cooling to room temperature, washed repeatedly with acetone and DI water, and finally freeze-dried to obtain PDAN-rGO [37].

PDAN-rGO-*x* composites were prepared by varying the ratio as follows: 1:2, 1:2.5, 1:1, 2.5:1, 5:1, 7.5:1, and 10:1.

Pristine PDAN was synthesized via chemical oxidative polymerization. Briefly, 0.2 g of 1,8-DAN was dissolved in 80 mL of DMF. Then, 0.5 g of APS in 100 mL of 0.1 M HCl was added dropwise to the mixture under vigorous stirring, maintaining the temperature below 0 °C. The polymerization proceeded for 12 h.

The resulting precipitate was collected by centrifugation, washed sequentially with DI water and acetone, and freeze-dried.

Subsequently, PDAN/rGO composite was prepared. Typically, pre-synthesized PDAN (0.1 g) was mixed with a GO suspension (0.02 g) and ultrasonicated for 30 min. The mixture underwent hydrothermal treatment in a Teflon-lined autoclave at 180 °C for 12 h. The product was collected, washed, and dried following the same procedures as pristine PDAN.

2.3 Material characterization

The morphology of the composites was observed by scanning electron microscopy (SEM, Hitachi S4800) and transmission electron microscopy (TEM, Talos 200c). Fourier transform infrared (FT-IR, Thermo Fisher Nicolet iS5) spectra were recorded from 400 to 4000 cm^{-1}. The chemical states of elements in PDAN and PDAN-rGO composites were analyzed by X-ray photoelectron spectroscopy (XPS, PHI-5702). *In situ* FT-IR measurements were performed using a Nicolet Nexus 670 spectrometer. *In situ* Raman spectroscopy was performed on a LabRAM HR Evolution spectrometer using an excitation laser wavelength of 473 nm.

2.4 Electrochemical measurements

The cathode slurry was prepared by mixing PDAN-rGO, acetylene black, and PVDF in a mass ratio of 6:2:2 in DMF. It was coated onto carbon paper (diameter: 10 mm and thickness: 1.5 mm) and dried to form the cathode. The typical active material loading was about 1.5 $mg{\cdot}cm^{-2}$. Higher mass loadings (about 7.18 $mg{\cdot}cm^{-2}$) were achieved by pressing a film composed of PDAN-rGO, acetylene black, and PTFE in a 6:2:2 ratio. ZIB coin batteries were assembled using the as-prepared cathode, zinc foil anode, and glass fiber separator, with 2 M $Zn(OTF)_2$ (OTF refers to trifluoromethanesulfonate) as the electrolyte. Cyclic voltammetry (CV) was recorded on a CHI 660E electrochemical workstation from 0 to 1.7 V at scan rates of 1–5 $mV{\cdot}s^{-1}$ for kinetic analysis. Electrochemical impedance spectroscopy (EIS) measurements were conducted over a frequency range of 0.01 to 100,000 Hz. Galvanostatic charge–discharge (GCD) tests were performed using a LAND testing system (CT3004A) at current densities ranging from 0.1 to 20 $A{\cdot}g^{-1}$ to evaluate rate capability and cycling stability.

3 Results and discussion

The PDAN-rGO composite was synthesized through *in situ* chemical oxidation polymerization of 1,8-DAN on graphene sheets. The anticipated structure of the resulting graphene-based polymer composite and its energy storage mechanism in 2 M $Zn(OTF)_2$ electrolyte are illustrated in Fig. 1. The PDAN-rGO structure features abundant imine (=N–) and amine (–NH–) groups, which serve as the primary active sites for electrochemical reactions. The extensive conjugated system of graphene contributes a high number of delocalized electrons, significantly enhancing the electrical conductivity of the composite [38].

The morphology and microstructure of the PDAN-rGO composite were characterized by SEM (Fig. 2(a) and Fig. S1 in the Electronic Supplementary Material (ESM)) and TEM (Fig. 2(b) and Fig. S2 in the ESM). Unlike pure PDAN, which forms severely agglomerated spherical particles that limit its electrochemical performance (Figs. S1(i) and S2(i) in the ESM), the PDAN-rGO

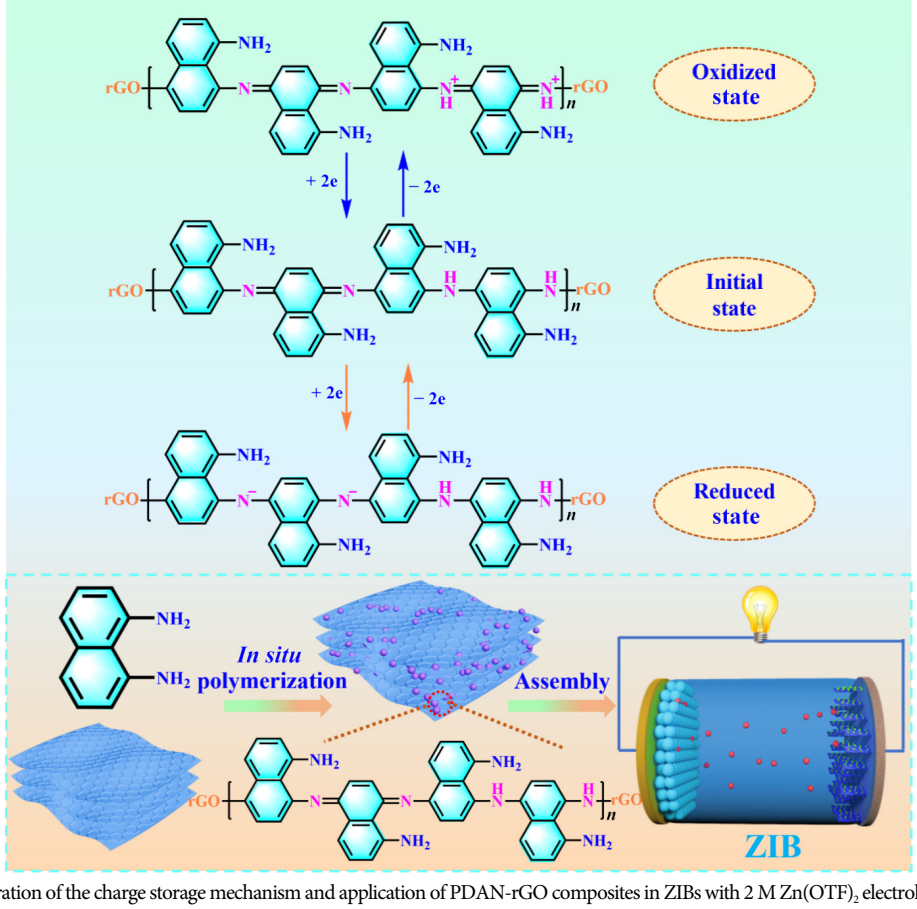

Figure 1 Schematic illustration of the charge storage mechanism and application of PDAN-rGO composites in ZIBs with 2 M $Zn(OTF)_2$ electrolyte.

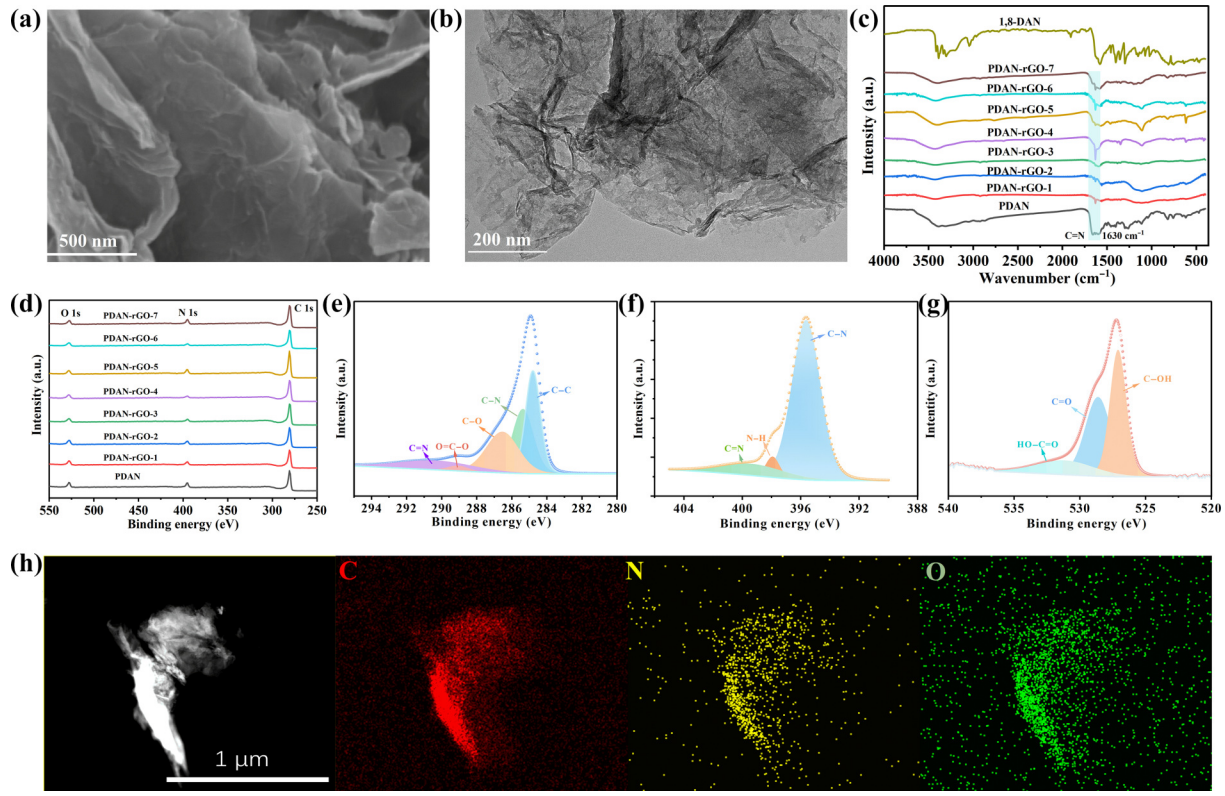

Figure 2 (a) SEM image and (b) TEM image of PDAN-rGO-5. (c) FT-IR spectra of PDAN-rGO. (d) XPS spectra of PDAN-rGO. ((e)–(g)) High-resolution spectra of (e) C 1s, (f) N 1s, and (g) O 1s. (h) TEM image of PDAN-rGO-5 and the corresponding EDS mapping of C, N, and O element distributions on PDAN-rGO-5.

composite exhibits a dominant graphene-like layered structure, in which the graphene framework effectively inhibits the agglomeration of PDAN. Furthermore, the uniform distribution of C, N, and O elements, as confirmed by energy dispersive X-ray spectroscopy (EDS) mapping (Fig. 2(h)), verifies the homogeneous anchoring of PDAN (N signal) on the graphene sheets, which contain residual oxygen-containing groups (O signal). This unique architecture is expected to significantly enhance the electrical conductivity of the PDAN-rGO composite.

FT-IR spectroscopy was employed to characterize the chemical structures of PDAN-rGO composites with different mass ratios (Fig. 2(c)). The spectra show characteristic absorption bands at approximately 3100 cm^{-1} (N–H stretching), 1630 cm^{-1} (C=N stretching), 1600 cm^{-1} (C=C/C=O vibrations and N–H bending), and 1270 cm^{-1} (C–N stretching), as well as at 1043, 816, and 758 cm^{-1} (C–H bending modes) [39]. XPS analysis further confirms the successful polymerization of 1,8-DAN on the graphene substrate, as evidenced by the presence of C 1s, N 1s, and O 1s in XPS spectra (Fig. 2(d)). The high-resolution C 1s spectra can be deconvoluted into five components located at binding energies of approximately 284.8 eV (C–C/C=C), 285.4 eV (C–N), 286.5 eV (C–O), 289.0 eV (O–C=O), and 290.6 eV (C=N/C=O) (Fig. 2(e)). The N 1s spectrum exhibits three fitted peaks centered at 395.7 eV (C–N), 397.9 eV (N–H), and 399.7 eV (C=N) (Fig. 2(f)), indicating the presence of different nitrogen environments consistent with the PDAN structure. The O 1s spectrum reveals contributions from C–OH (527.2 eV), C=O (528.6 eV), and HO–C=O (531.1 eV) (Fig. 2(g)), suggesting that oxygen-containing functional groups are partially retained in the rGO framework after hydrothermal treatment [40]. The coexistence of these bonding states, particularly the C=N and C–N species in both C 1s and N 1s spectra, provides clear evidence for the successful formation of PDAN-rGO composites [41].

The electrochemical performance of the PDAN-rGO-*x* composites was evaluated as cathode materials in Zn//PDAN-rGO-*x* half-cells with 2 M $Zn(OTF)_2$ aqueous electrolyte. CV measurements were conducted at scan rates ranging from 1 to 5 $mV \cdot s^{-1}$ (Fig. 3(a) and Figs. S3(a), S4(a), S5(a), S6(a), S7(a), S8(a), and S9(a) in the ESM). All CV curves exhibit a pair of reversible redox peaks centered at approximately 1.01 and 0.68 V, which can be attributed to the reversible Zn^{2+} insertion/extraction (n-type behavior) of the composite. As the voltage approaches 1.7 V, the CV curves evolve into a more rectangular shape, suggesting an increasing contribution of capacitive charge storage. This behavior is associated with the surface adsorption/desorption of $CF_3SO_3^-$ anions (p-type behavior) on the electrode. GCD tests were carried out at various current densities ranging from 0.1 to 20 $A \cdot g^{-1}$ (Figs. S3(b), S4(b), S5(b), S6(b), S7(b), S8(b), and S9(b) in the ESM). Among all composites, PDAN-rGO-5 exhibits the highest specific capacity of 162.7 $mAh \cdot g^{-1}$ at 0.1 $A \cdot g^{-1}$ (Figs. 3(b) and 3(c)). Remarkably, it still delivers 101.01 $mAh \cdot g^{-1}$ at 20 $A \cdot g^{-1}$, demonstrating excellent rate capability. When the current density is switched back to 0.1 $A \cdot g^{-1}$, the capacity returns to its original value, underscoring outstanding electrochemical reversibility. This superior performance is further corroborated by EIS analysis (Fig. S10 in the ESM). The Nyquist plot of PDAN-rGO-5 shows a significantly smaller semicircle diameter. The corresponding charge transfer resistance (R_{ct}) is calculated to be 101.6 Ω, markedly lower than that of the control. This minimized resistance indicates superior electron and ion transport efficiency, directly contributing to its outstanding electrochemical performance. The superior performance of PDAN-rGO-5 is attributed to its porous structure,

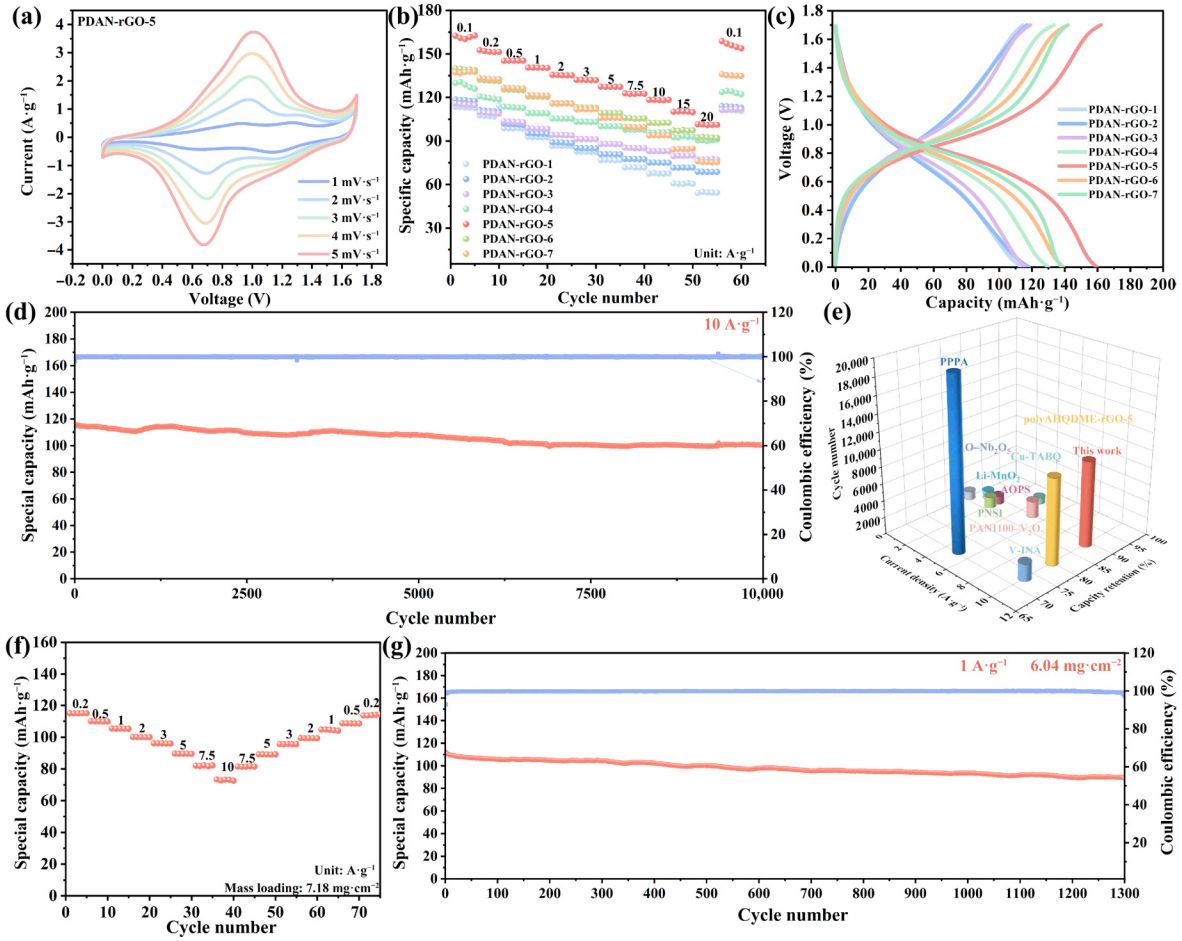

Figure 3 (a) CV curves of PDAN-rGO-5 from 1 to 5 mV·s^{-1}. (b) Rate performance of PDAN-rGO-*x*. (c) GCD curves of PDAN-rGO-*x* at 0.1 A·g^{-1}. (d) Cycle stability of PDAN-rGO-5 at 10 A·g^{-1}. (e) Comparison of cycle performance between PDAN-rGO-5 and some recently reported organic cathodes. (f) Rate performance of PDAN-rGO-5 at 7.18 mg·cm^{-2}. (g) Cycle stability of PDAN-rGO-5 at 1 A·g^{-1} with high mass-loading.

enabled by rGO incorporation, which facilitates efficient Zn^{2+} diffusion and rapid charge transfer, thus improving zinc storage kinetics [42].

To elucidate the synergistic effect within the composite, control experiments were performed on pristine components and a mixed preparation sample (Figs. S11–S14 in the ESM). Pristine rGO and PDAN delivered limited capacities of 69 and 34 mAh·g^{-1} at 0.1 A·g^{-1}, respectively. Moreover, the PDAN/rGO control yielded a capacity of only 118 mAh·g^{-1}, confirming that the intimate molecular-level contact facilitated by *in situ* polymerization is critical for maximizing electrochemical performance. The Ragone plot demonstrates that the Zn//PDAN-rGO-5 battery achieves a high energy density of 120.97 Wh·kg^{-1} at a power density of 75.42 W·kg^{-1} (Fig. S15 in the ESM). Furthermore, the PDAN-rGO-5 exhibits exceptional long-term cycling stability, retaining 89.18% of its capacity (100.73 mAh·g^{-1}) after 10,000 cycles at 10 A·g^{-1} (Fig. 3(d)). GCD curves recorded at the 1000th, 5000th, and 10,000th cycles (Fig. S16 in the ESM) display highly consistent voltage plateaus, verifying the robust redox reversibility of the material. This outstanding durability suggests excellent structural stability, surpassing that of many recently reported ZIB cathodes (Fig. 3(e)) [33, 43–51]. Additionally, the practical potential of PDAN-rGO-5 was examined using high mass-loading electrodes (~ 7.18 mg·cm^{-2}). The electrode delivers a specific capacity of 115 mAh·g^{-1} at 0.2 A·g^{-1} (Fig. 3(f)). Impressively, it retains ~ 75% of this capacity even at 10 A·g^{-1} and recovers to ~ 116 mAh·g^{-1} when the current is restored to 0.2 A·g^{-1}, demonstrating excellent kinetic stability. Long-term cycling at 1 A·g^{-1} further confirms its durability, with a capacity retention of 73.64% (82.5 mAh·g^{-1}) after 1400 cycles (Fig. 3(g)).

With its high capacity, excellent rate performance, and long-term cycling stability, PDAN-rGO-5 demonstrates great potential as a cathode material for advanced aqueous ZIB. The electrochemical kinetics of the PDAN-rGO-5 composite cathode were systematically investigated to elucidate its charge storage mechanism. As the scan rate increases from 0.2 to 1 mV·s^{-1}, the PDAN-rGO-5 cathode exhibits only a minimal peak shift, demonstrating excellent electrochemical reversibility (Fig. 4(a)). The *b*-values derived from the relationship $i = av^b$, where i is the peak current, v is the scan rate, and a and b are empirical parameters. As shown in Fig. 4(b), the b values were calculated to be 0.881 for the anodic peak and 0.886 for the cathodic peak, suggesting that the charge-storage process is predominantly capacitive-controlled. In contrast, the *b*-value of pure PDAN was significantly lower (0.679 and 0.514), suggesting slower kinetics and a more diffusion-limited process (Fig. S12 in the ESM). This comparison highlights the critical role of graphene in enhancing the reaction kinetics of the composite. To further quantify the contribution of capacitive and diffusion-controlled processes, the current response was deconvoluted using the equation $i = k_1v + k_2v^{0.5}$, where k_1 and k_2 are constants. Here, k_1v and $k_2v^{0.5}$ represent the current contributions

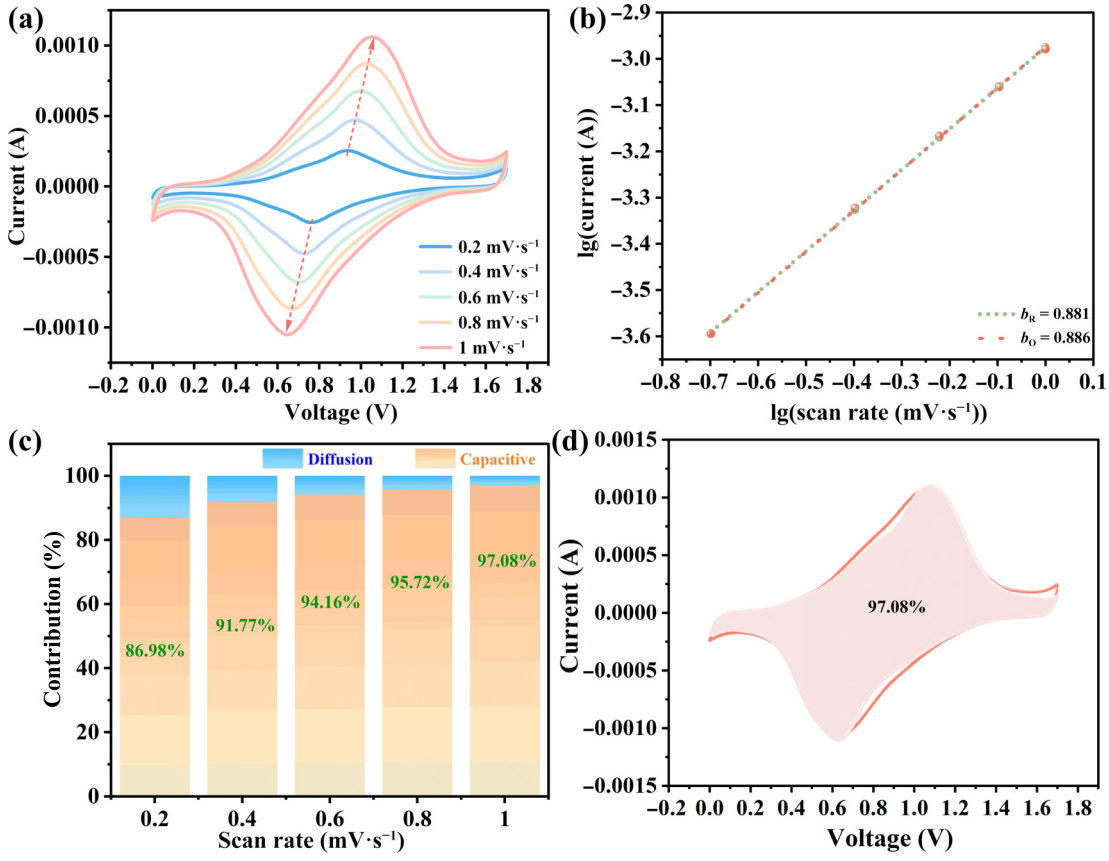

Figure 4 (a) CV curves of Zn//PDAN-rGO-5 from 0.2 to 1 mV·s^{-1}. (b) The linear logarithm relationships between anodic and cathodic peak current versus the scan rate of CV curve. (c) Capacitive distribution ratios. (d) Capacitive distribution ratios at 1 mV·s^{-1}.

from capacitive and diffusion processes, respectively. The capacitive contribution increased from 86.98% to 97.08% as the scan rate rose from 0.2 to 1 mV·s^{-1} (Figs. 4(c) and 4(d)), confirming the highly surface-driven behavior of PDAN-rGO-5. Such prominent capacitive characteristic facilitates efficient ion transport and rapid reaction kinetics, which are responsible for the excellent rate performance of the Zn//PDAN-rGO-5 batteries. It is worth noting that the capacity is primarily contributed by the n-type (Zn^{2+} storage) reaction (Fig. S17 in the ESM), whereas the p-type ($CF_3SO_3^-$ storage) reaction accounts for only a minor portion (10.79%). Furthermore, galvanostatic intermittent titration technique (GITT) measurements (Fig. S18 in the ESM) were conducted to determine the Zn^{2+} diffusion coefficients ($D_{Zn^{2+}}$). The calculated $D_{Zn^{2+}}$ values range from 10^{-10} to 10^{-9} cm^2·s^{-1} throughout the charge/discharge process, further confirming that the conductive rGO network enables efficient ion diffusion and superior rate capability.

Density functional theory (DFT) calculations were conducted to investigate the electronic properties and the electrochemical evolution of PDAN during electrochemical process. The energy gap (ΔE) between the highest occupied molecular orbital (HOMO) and the lowest unoccupied molecular orbital (LUMO) was calculated to be 2.11 eV (Fig. 5(a)), indicating semiconductor-like behavior that supports electron transport in the electrode [52, 53]. The molecular electrostatic potential (MESP) surface reveals distinct charge distributions: electron-rich (blue) regions correspond to C=N groups (Fig. 5(b)), which serve as active sites for Zn^{2+} uptake during discharge, while electron-deficient (red) regions around –NH– moieties facilitate $CF_3SO_3^-$ adsorption during charging. Geometry optimization confirms the formation of a $PDAN_2(Zn^{2+})_2$ complex in the discharged state, where Zn^{2+} ions bridge adjacent PDAN chains. Thermodynamically, the binding Gibbs free energy change ($\Delta G_{binding}$) for the formation of PDAN(Zn^{2+}) is –1.41 eV, indicating a spontaneous discharge process, whereas the $\Delta G_{binding}$ for $CF_3SO_3^-$ adsorption is +0.52 eV, consistent with an endergonic charging step (Fig. 5(b) and Table S1 in the ESM). These results corroborate the bipolar ion-storage behavior of PDAN.

In situ Raman and FT-IR spectroscopy were performed to clarify the energy storage mechanism of the PDAN-rGO composite. The *in situ* Raman measurements were conducted using GCD curves at 0.1 A·g^{-1} (Fig. 5(c)). *In situ* Raman spectra show that the intensity of the C=N vibration peak at 1441 cm^{-1} decreases upon discharge and recovers during charging (Figs. 5(d) and 5(e)), indicating that the C=N group acts as a redox-active center. This reversible change was further confirmed by *in situ* FT-IR analysis (Fig. 5(g)), which utilized CV curves at 1 mV·s^{-1} (Fig. 5(f)). During discharge, the intensities of the C–N (1225 cm^{-1}) and aromatic C–H (1085 cm^{-1}) stretching vibrations increase, suggesting the conversion of C=N in non-aromatic rings to C–N in aromatic rings. Upon charging, these peaks diminish, demonstrating high reversibility of the redox process.

Additionally, the PDAN-rGO-5 composite demonstrates excellent Zn^{2+} storage performance. It also exhibits a unique capability for spontaneous self-charging in air. Mechanistically, the charging process involves the oxidation of the cathode, accompanied by the extraction of Zn^{2+} ions to maintain charge neutrality. While this is typically driven by an external power supply, it can also occur chemically if a suitable oxidant provides a

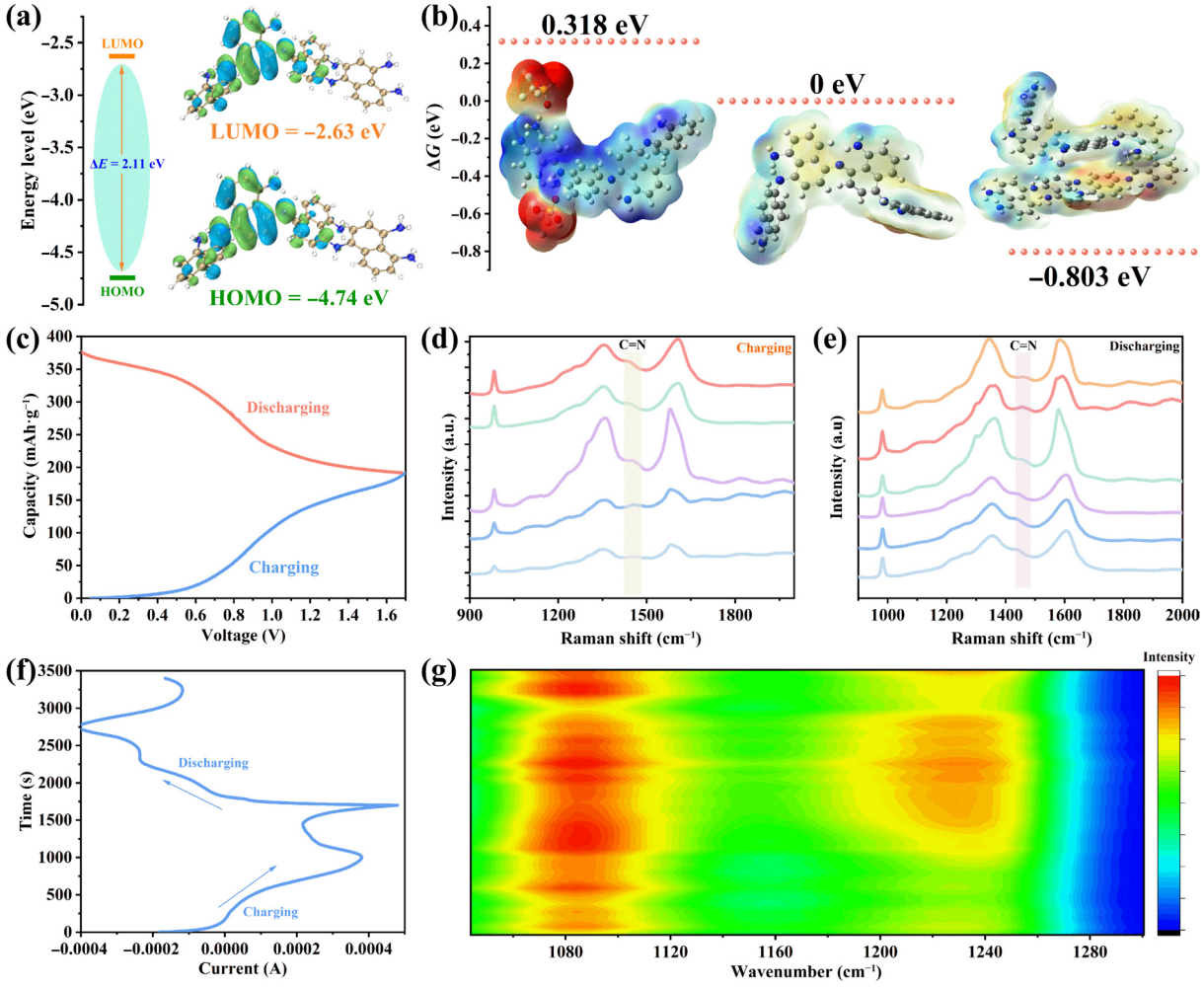

Figure 5 (a) Optimized structure and calculated frontier molecular orbital energy of PDAN. (b) $\Delta G_{binding}$ of PDAN molecules upon binding with Zn^{2+} cations and $CF_3SO_3^-$ anions and calculated MESP distributions of PDAN, $PDAN_2(Zn^{2+})_2$, and $PDAN(CF_3SO_3^-)_2$ complexes. (c) GCD curves at 0.1 A·g^{-1}. ((d) and (e)) *In situ* Raman spectra. (f) CV curve at 1 mV·s^{-1}. (g) *In situ* FT-IR spectra.

thermodynamic driving force [54]. To validate this theoretical feasibility, the redox potentials were analyzed. As shown in Fig. 3(a), the reduction potential of PDAN-rGO-5 is 0.65 V vs. Zn^{2+}/Zn. According to the Nernst equation, this corresponds to −0.11 V vs. SHE. In contrast, oxygen (O_2), which is abundant in ambient air, possesses a standard electrode potential (E^0) of approximately 0.40 V (neutral medium) to 1.23 V (acidic medium) vs. SHE [55]. Since the reduction potential of O_2 is significantly higher than the oxidation potential of PDAN-rGO-5 (−0.11 V), oxygen can spontaneously accept electrons from the discharged cathode. Consequently, the PDAN-rGO-5 is chemically oxidized, and Zn^{2+} ions are extracted from the cathode matrix without external energy input until the system reaches equilibrium (Fig. 6(a)).

To evaluate this property, Zn//PDAN-rGO-5 batteries were assembled and subjected to self-charging tests. Figure 6(c) illustrates the OCV recovery of a fully discharged battery exposed to air. The OCV rapidly recovered to 1.2 V within 5 h and eventually saturated at 1.25 V after 10 h. This rapid voltage recovery places the PDAN-rGO-5 composite among the state-of-the-art materials for self-charging ZIBs [23, 56–59]. The efficiency and rate capability of the self-charged battery were further assessed by discharging the battery after a 10 h self-charging period (Fig. 6(b)). At 0.2 A·g^{-1}, the battery delivered a specific capacity of 144.21 mAh·g^{-1}, which corresponds to 95.2% of the capacity obtained via galvanostatic charging (151.47 mAh·g^{-1}). The high capacity retention suggests that the majority of the redox-active sites in PDAN-rGO-5 are effectively oxidized by atmospheric oxygen. Furthermore, the battery exhibited excellent rate capability, delivering capacities of 90.63, 74.63, 59.0, 48.5, 39.4, and 27.2 mAh·g^{-1} at current densities of 0.5, 1, 2, 3, 5, and 10 A·g^{-1}, respectively. The self-charging efficiency was evaluated by comparing discharge profiles with those from conventional electrochemical charging at 0.2 A·g^{-1} (Fig. S19 in the ESM). The self-charged battery exhibits a slightly lower voltage plateau, attributed to thermodynamic/kinetic limitations and polarization losses at the solid–liquid–gas three-phase interface. Nevertheless, PDAN-rGO-5 successfully recovers most of its discharge capacity while maintaining a stable voltage plateau, demonstrating its robust self-charging capability. To elucidate the synergistic mechanism, control experiments were conducted on pristine PDAN and rGO (Fig. S20 in the ESM). Although pristine PDAN exhibits intrinsic redox plateaus, it delivers a limited capacity of 40.7 mAh·g^{-1} at 0.2 A·g^{-1} and suffers from poor structural stability due to the absence of a conductive skeleton. Consequently, the electrode degrades rapidly after high-rate cycling (10 A·g^{-1}), resulting in self-charging failure. Conversely, pristine

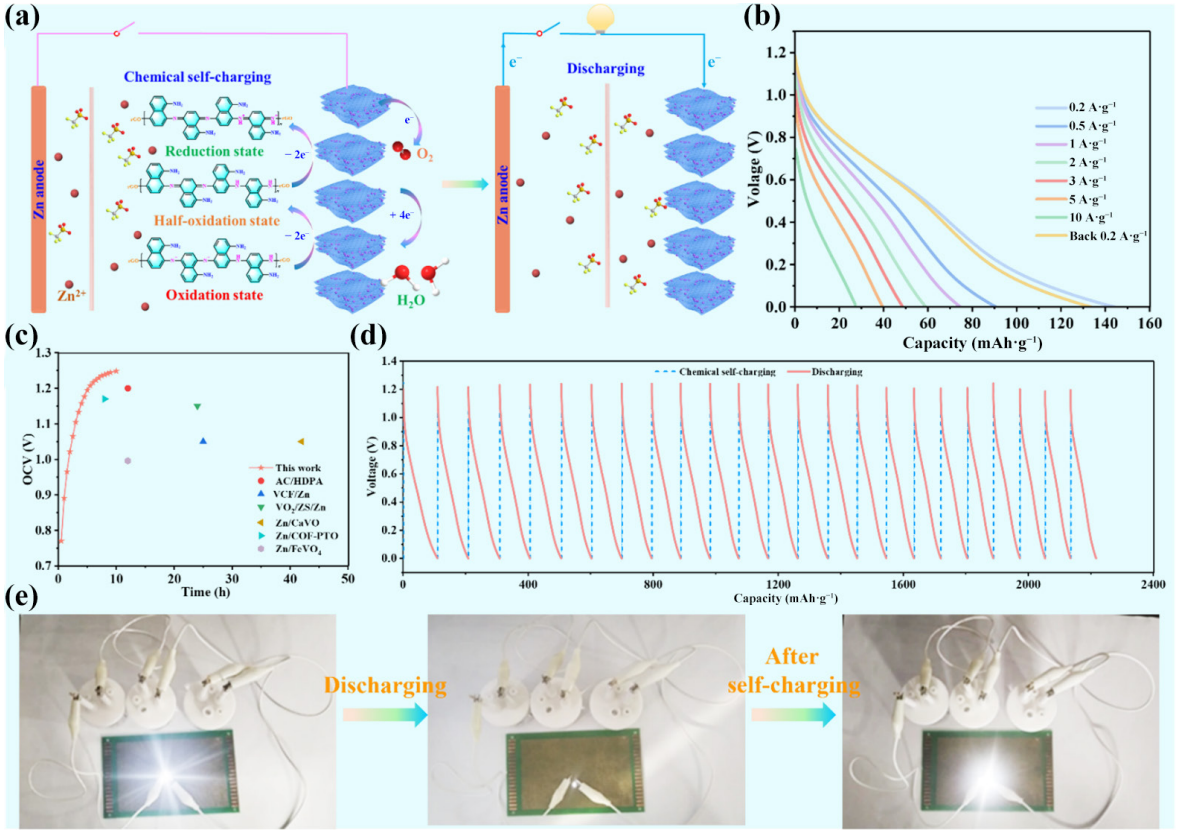

Figure 6 (a) Chemical self-charging mechanism of Zn//PDAN-rGO battery. (b) Discharge curves of Zn//PDAN-rGO batteries after fully self-charging at different current densities. (c) Self-charging curve of Zn//PDAN-rGO. (d) Self-charging cycling stability of Zn//PDAN-rGO electrodes. (e) LEDs are powered by three-self-charging Zn//PDAN-rGO battery.

rGO yields a capacity of 69.8 mAh·g^{-1} at 0.2 A·g^{-1} but displays a linear, capacitive discharge profile devoid of voltage plateaus, reflecting its lack of redox centers. This contrast highlights the critical synergy within the composite, where the rGO network is essential for maintaining the structural integrity and electrical conductivity required for stable, reversible self-charging.

The long-term stability of the chemical self-charging process was evaluated by repeating a cycle of galvanostatic discharge (to 0 V at 0.5 A·g^{-1}) followed by a 10 h rest for self-charging (Fig. 6(d)). Over 20 consecutive cycles, the self-charged voltage consistently reached > 1.2 V, and the device achieved an impressive cumulative specific discharge capacity of 2135.08 mAh·g^{-1}. To underscore the practical viability of the device, three Zn//PDAN-rGO-5 batteries were connected in series to power a white light-emitting diode (LED) array (Fig. 6(e)). Following a prolonged discharge period where the LEDs gradually dimmed (Movie S1 in the ESM), the batteries underwent an air-assisted self-charging process for approximately 10 h. Remarkably, the regenerated batteries were able to light the LED array with high intensity and sustain operation for an extended duration (Fig. 6(e) and Movies S2 and S3 in the ESM). These results robustly validate the potential of Zn//PDAN-rGO-5 batteries for sustainable, self-powered energy storage applications.

4 Conclusions

In summary, a bipolar PDAN-rGO composite has been successfully developed as a high-performance cathode for aqueous ZIBs. The charge storage mechanism, elucidated through DFT calculations and *in situ* Raman/FTIR spectroscopy, involves reversible Zn^{2+} storage at C=N sites and $CF_3SO_3^-$ adsorption at –NH– groups, demonstrating a dual-ion storage behavior. The composite exhibits outstanding electrochemical performance, including excellent rate capability and long-term cycling stability (89.18% capacity retention after 10,000 cycles), attributed to the conductive graphene framework and robust polymer structure. Notably, the PDAN-rGO cathode can be spontaneously oxidized by atmospheric oxygen due to its favorable redox potential, enabling an efficient self-charging function that achieves an OCV of 1.25 V and a cumulative discharge capacity of 2216.6 mAh·g^{-1}. Practical feasibility is confirmed by powering LEDs through self-charging cycles. This work offers a feasible strategy for designing bipolar organic electrodes and advances the development of self-sustaining zinc-ion batteries with air-harvesting functionality.

Electronic Supplementary Material: Supplementary material (SEM and TEM images, CV and GCD curves, EIS, rate capability, Ragone plot, GITT curve, and self-charging performance of PDAN and rGO) is available in the online version of this article at https://doi.org/10.26599/NR.2026.94908674.

Data availability

All data needed to support the conclusions in the paper are presented in the manuscript and the Electronic Supplementary Material. Additional data related to this paper may be requested from the corresponding author upon request.

Acknowledgements

The authors would like to acknowledge the financial support from the National Natural Science Foundation of China (No. 22005127), Gansu Province Youth Talent (Team Project, No. 2025QNTD57), and Gansu Province Higher Education Teachers' Innovation Fund Project (No. 2025B-015). All the theoretical calculations were performed at the Supercomputing Center of Lanzhou University.

Declaration of competing interest

All the contributing authors report no conflict of interests in this work.

Author contribution statement

Y. Q. M.: Data curation, conceptualization, investigation, writing – original draft. S. P. Y.: Data curation, methodology, writing – original draft. S. M. G.: Software, formal analysis, data curation. J. J. H.: Investigation, formal analysis. Y. J. G.: Investigation, formal analysis. Y. X. Y.: Investigation, formal analysis. P. C. D.: Writing – review & editing, supervision, funding acquisition, conceptual. All the authors have approved the final manuscript.

Use of AI statement

None.

References

[1] Dincer, I. Renewable energy and sustainable development: A crucial review. *Renew. Sustain. Energy Rev.* **2000**, *4*, 157–175.

[2] Turner, J. M. The matter of a clean energy future. *Science* **2022**, *376*, 1361.

[3] Yu, L. P.; Chen, G. Z. Supercapatteries as high-performance electrochemical energy storage devices. *Electrochem. Energy Rev.* **2020**, *3*, 271–285.

[4] Lu, J.; Wu, T. P.; Amine, K. State-of-the-art characterization techniques for advanced lithium-ion batteries. *Nat. Energy* **2017**, *2*, 17011.

[5] Hwang, J. Y.; Myung, S. T.; Sun, Y. K. Sodium-ion batteries: Present and future. *Chem. Soc. Rev.* **2017**, *46*, 3529–3614.

[6] Quilty, C. D.; Wu, D. R.; Li, W. Z.; Bock, D. C.; Wang, L.; Housel, L. M.; Abraham, A.; Takeuchi, K. J.; Marschilok, A. C.; Takeuchi, E. S. Electron and ion transport in lithium and lithium-ion battery negative and positive composite electrodes. *Chem. Rev.* **2023**, *123*, 1327–1363.

[7] Tang, B. Y.; Shan, L. T.; Liang, S. Q.; Zhou, J. Issues and opportunities facing aqueous zinc-ion batteries. *Energy Environ. Sci.* **2019**, *12*, 3288–3304.

[8] Yu, H. Q.; Wang, L.; Zhang, Z. G.; Li, Y. D.; Yang, S. C.; He, X. M. Insight understanding of external pressure on lithium plating in commercial lithium-ion batteries. *Adv. Funct. Mater.* **2024**, *34*, 2406966.

[9] Lu, Y.; Chen, J. Prospects of organic electrode materials for practical lithium batteries. *Nat. Rev. Chem.* **2020**, *4*, 127–142.

[10] Song, M.; Tan, H.; Chao, D. L.; Fan, H. J. Recent advances in Zn-ion batteries. *Adv. Funct. Mater.* **2018**, *28*, 1802564.

[11] Wang, H. G.; Wu, Q.; Cheng, L. Q.; Zhu, G. S. The emerging aqueous zinc-organic battery. *Coord. Chem. Rev.* **2022**, *472*, 214772.

[12] Wang, Y. W.; Zhang, Y. X.; Gao, G.; Fan, Y. W.; Wang, R. X.; Feng, J.; Yang, L. N.; Meng, A. L.; Zhao, J.; Li, Z. J. Effectively modulating oxygen vacancies in flower-like δ-MnO_2 nanostructures for large capacity and high-rate zinc-ion storage. *Nano-Micro Lett.* **2023**, *15*, 219.

[13] Xiao, X. L.; Zhang, L.; Xin, W. L.; Yang, M.; Geng, Y. H.; Niu, M. F.; Zhang, H.; Zhu, Z. Q. Self-assembled layer of organic phosphonic acid enables highly stable MnO_2 cathode for aqueous Znic batteries. *Small* **2024**, *20*, 2309271.

[14] Jo, J. H.; Sun, Y. K.; Myung, S. T. Hollandite-type Al-doped $VO_{1.52}(OH)_{0.77}$ as a zinc ion insertion host material. *J. Mater. Chem. A* **2017**, *5*, 8367–8375.

[15] Zhang, H.; Peng, J.; Li, L.; Zhao, Y. N.; Gao, Y.; Wang, J. Z.; Cao, Y. L.; Dou, S. X.; Chou, S. L. Low-cost zinc substitution of iron-based Prussian blue analogs as long lifespan cathode materials for fast charging sodium-ion batteries. *Adv. Funct. Mater.* **2023**, *33*, 2210725.

[16] Alfaruqi, M. H.; Mathew, V.; Gim, J.; Kim, S.; Song, J. J.; Baboo, J. P.; Choi, S. H.; Kim, J. Electrochemically induced structural transformation in a γ-MnO_2 cathode of a high capacity zinc-ion battery system. *Chem. Mater.* **2015**, *27*, 3609–3620.

[17] Xie, X. S.; Fu, H. W.; Fang, Y.; Lu, B. G.; Zhou, J.; Liang, S. Q. Manipulating ion concentration to boost two-electron Mn^{4+}/Mn^{2+} redox kinetics through a colloid electrolyte for high-capacity zinc batteries. *Adv. Energy Mater.* **2022**, *12*, 2102393.

[18] Li, Z. L.; Ganapathy, S.; Xu, Y. L.; Zhou, Z.; Sarilar, M.; Wagemaker, M. Mechanistic insight into the electrochemical performance of Zn/VO_2 batteries with an aqueous $ZnSO_4$ electrolyte. *Adv. Energy Mater.* **2019**, *9*, 1900237.

[19] Cao, W. Z.; Lu, J. Z.; Zhou, K.; Sun, G. C.; Zheng, J.; Geng, Z.; Li, H. Organic–inorganic composite SEI for a stable Li metal anode by *in situ* polymerization. *Nano Energy* **2022**, *95*, 106983.

[20] Chao, D. L.; Zhu, C. R.; Song, M.; Liang, P.; Zhang, X.; Tiep, N. H.; Zhao, H. F.; Wang, J.; Wang, R. M.; Zhang, H. et al. A high-rate and stable quasi-solid-state zinc-ion battery with novel 2D layered zinc orthovanadate array. *Adv. Mater.* **2018**, *30*, 1803181.

[21] Tie, Z.; Liu, L. J.; Deng, S. Z.; Zhao, D. B.; Niu, Z. Q. Proton insertion chemistry of a zinc-organic battery. *Angew. Chem., Int. Ed.* **2020**, *59*, 4920–4924.

[22] Li, D. J.; Guo, Y. X.; Zhang, C. X.; Chen, X. H.; Zhang, W. S.; Mei, S. L.; Yao, C. J. Unveiling organic electrode materials in aqueous zinc-ion batteries: From structural design to electrochemical performance. *Nano-Micro Lett.* **2024**, *16*, 194.

[23] Yan, L.; Zhang, Y.; Ni, Z. G.; Zhang, Y.; Xu, J.; Kong, T. Y.; Huang, J. H.; Li, W.; Ma, J.; Wang, Y. G. Chemically self-charging aqueous zinc-organic battery. *J. Am. Chem. Soc.* **2021**, *143*, 15369–15377.

[24] Patil, N.; de la Cruz, C.; Ciurduc, D.; Mavrandonakis, A.; Palma, J.; Marcilla, R. An ultrahigh performance zinc-organic battery using poly(catechol) cathode in $Zn(TFSI)_2$-based concentrated aqueous electrolytes. *Adv. Energy Mater.* **2021**, *11*, 2100939.

[25] Qiu, X.; Wang, N.; Wang, Z.; Wang, F.; Wang, Y. G. Towards high-performance zinc-based hybrid supercapacitors via macropores-based charge storage in organic electrolytes. *Angew. Chem., Int. Ed.* **2021**, *60*, 9610–9617.

[26] Chen, D.; Lu, M. J.; Wang, B. R.; Cheng, H. F.; Yang, H.; Cai, D.; Han, W.; Fan, H. J. High-mass loading $V_3O_7{\cdot}H_2O$ nanoarray for Zn-ion battery: New synthesis and two-stage ion intercalation chemistry. *Nano Energy* **2021**, *83*, 105835.

[27] Jiao, T. P.; Yang, Q.; Wu, S. L.; Wang, Z. F.; Chen, D.; Shen, D.; Liu, B.; Cheng, J. Y.; Li, H. F.; Ma, L. T. et al. Binder-free hierarchical VS_2 electrodes for high-performance aqueous Zn ion batteries towards commercial level mass loading. *J. Mater. Chem. A* **2019**, *7*, 16330–16338.

[28] Ma, L. W.; Wang, X. Y.; Sun, J. C. A strategy associated with conductive binder and 3D current collector for aqueous zinc-ion batteries with high mass loading. *J. Electroanal. Chem.* **2020**, *873*, 114395.

[29] Guo, J. C.; Pan, L. M.; Sun, J.; Wei, D. B.; Dai, Q. X.; Xu, J. H.; Li, Q. L.; Han, M. S.; Wei, L.; Zhao, T. S. Metal-free fabrication of nitrogen-doped vertical graphene on graphite felt electrodes with

enhanced reaction kinetics and mass transport for high-performance redox flow batteries. *Adv. Energy Mater.* **2024**, *14*, 2302521.
[30] Li, Y. Q.; Zhang, X. N.; Gan, M.; Sha, J. B.; Zhang, Y. G.; Liu, J. Z. An air-rechargeable Zn-organic battery with unprecedented fast self-charging rate. *Chem. Eng. J.* **2024**, *500*, 157022.
[31] Song, Y. F.; Qin, Q. H.; Jing, L. Y.; Li, M.; Zhao, H.; Cui, J. X.; Zhang, Y. Q. Design and construction of poly(benzoquinone-diamine)/$Ti_3C_2T_x$ hybrid electrode toward advanced aqueous zinc-ion batteries. *Compos. B: Eng.* **2023**, *252*, 110517.
[32] Li, S. Y.; Zhao, L. P.; Zheng, R. R.; Fan, G. L.; Liu, L. S.; Zhou, X.; Chen, X. T.; Qiu, X. Z.; Yu, X. Y.; Cheng, H. Tumor microenvironment adaptable nanoplatform for O_2 self-sufficient chemo/photodynamic combination therapy. *Part. Part. Syst. Charact.* **2020**, *37*, 1900496.
[33] Wang, Y. X.; Cui, H. L.; Li, R.; Yue, C. C.; Pan, H. C.; Tang, Z. J.; Wang, X. K.; Lin, Y. L.; Li, H. F.; Han, C. P. et al. Bistate-type ion storage of azo polymer for aqueous zinc ion battery. *Energy Storage Mater.* **2024**, *65*, 103102.
[34] Xu, Q. J.; Zhang, X. X.; Yuan, X. C.; Zhang, W. X.; Li, Y. Q.; Zhang, Y. G.; Liu, J. Z. A high-capacity and high-voltage aqueous Zn-polymer battery with self-charging function. *Adv. Energy Mater.* **2024**, *14*, 2303475.
[35] Tie, Z.; Zhang, Y.; Zhu, J. C.; Bi, S. S.; Niu, Z. Q. An air-rechargeable Zn/organic battery with proton storage. *J. Am. Chem. Soc.* **2022**, *144*, 10301–10308.
[36] Su, W.; Zhang, Y.; Wang, H. M.; Yang, M.; Niu, Z. Q. An ultrafast air self-charging zinc battery. *Adv. Mater.* **2024**, *36*, 2308042.
[37] Yan, L.; Zhu, Q.; Qi, Y. E.; Xu, J.; Peng, Y.; Shu, J.; Ma, J.; Wang, Y. G. Towards high-performance aqueous zinc batteries via a semi-conductive bipolar-type polymer cathode. *Angew. Chem., Int. Ed.* **2022**, *61*, e202211107.
[38] Geim, A. K. Graphene: Status and prospects. *Science* **2009**, *324*, 1530–1534.
[39] da Silva, Q. G.; Vieira Barbosa, N.; de Pieri Troiani, E.; Censi Faria, R. Electrochemical determination of norepinephrine on cathodically pretreated poly(1,5-diaminonaphthalene) modified electrode. *Electroanalysis* **2011**, *23*, 1359–1364.
[40] Tu, Z. Y.; Xie, Z. X.; Zhou, Q. H.; He, J.; Dong, Y. Y.; Huang, C. Z.; Zhang, F.; Zheng, Q. B.; Zhang, Y. H. *In situ* polymerization of multifunctional heat-resisting SiC-induced graphene/polyimide bidirectional thermally conductive film for battery thermal management. *Compos. Part A: Appl. Sci. Manuf.* **2025**, *199*, 109178.
[41] Wang, N.; Zhou, R. K.; Li, H.; Zheng, Z. L.; Song, W. X.; Xin, T.; Hu, M. J.; Liu, J. Z. New insights into the electrochemistry of carbonyl- and amino-containing polymers for rechargeable zinc-organic batteries. *ACS Energy Lett.* **2021**, *6*, 1141–1147.
[42] Rathore, H. K.; Das, C.; Biswas, G.; Kumar, M.; Sankhala, S. K.; Sarkar, D. Cerium oxide nanoparticles decorated on graphene oxide nanosheets as battery-type cathode material for supercapacitors. *J. Colloid Interface Sci.* **2025**, *685*, 280–290.
[43] Ye, F.; Liu, Q.; Dong, H. L.; Guan, K. L.; Chen, Z. Y.; Ju, N.; Hu, L. F. Organic zinc-ion battery: Planar, π-conjugated quinone-based polymer endows ultrafast ion diffusion kinetics. *Angew. Chem., Int. Ed.* **2022**, *61*, e202214244.
[44] Zhang, C. H.; Luo, Y.; Chang, S. L.; Wu, J. P.; Zhang, P.; Zhao, F. G. High-performance aqueous zinc-ion batteries enabled by graphene electrode modified with multiple redox polymer. *J. Electroanal. Chem.* **2025**, *981*, 118962.
[45] Mao, S. J.; Wu, Y.; Xu, S. R.; Xiao, T. Y.; Li, Y. Y.; Li, Z. K.; Pan, X. F.; Yuan, B.; Xu, Y. F.; Wen, H. et al. Design of large-spacing, high-stability PANI-$Ni_xV_2O_5$ nanobelts as cathode for aqueous zinc-ion batteries using an organic–inorganic co-embedding strategy. *J. Power Sources* **2025**, *628*, 235912.
[46] Chen, S.; Li, K.; Hui, K. S.; Zhang, J. T. Regulation of lamellar structure of vanadium oxide via polyaniline intercalation for high-performance aqueous zinc-ion battery. *Adv. Funct. Mater.* **2020**, *30*, 2003890.
[47] Kamenskii, M. A.; Volkov, F. S.; Eliseeva, S. N.; Tolstopyatova, E. G.; Kondratiev, V. V. Enhancement of electrochemical performance of aqueous zinc ion batteries by structural and interfacial design of MnO_2 cathodes: The metal ion doping and introduction of conducting polymers. *Energies* **2023**, *16*, 3221.
[48] Zhou, C. S.; Lai, S. M.; Chen, Z.; Lin, K. J.; Tan, Y. M.; Yao, H.; Yang, Y. Y. Coordination structures integrating multiple redox-active centers for enhanced zinc-ion storage. *ACS Appl. Energy Mater.* **2025**, *8*, 1078–1088.
[49] Zhang, J. H.; Zhang, X. J.; Cui, S. H.; Zhang, Y. H.; Wang, K. Oxygen vacancy-enriched Nb_2O_5 as a low-potential insertion anode for high-performance zinc-ion batteries: Mechanistic insights and electrochemical enhancements. *Electrochim. Acta* **2025**, *524*, 146001.
[50] Xu, D. X.; Zhang, H.; Cao, Z. Y.; Wang, L. P.; Ye, Z. L.; Chen, B.; Li, X. Y.; Zhu, X. D.; Ye, M. X.; Shen, J. F. High-rate aqueous zinc-ion batteries enabled by a polymer/graphene composite cathode involving reversible electrolyte anion doping/dedoping. *J. Mater. Chem. A* **2021**, *9*, 10666–10671.
[51] Ma, F. Y.; Yu, J. M.; Pu, Y. X.; Wang, S. J.; Gong, X. F.; Li, S. H.; Chen, J. W. Redox-active polymer/graphene composite anode for advanced aqueous zinc-ion batteries. *Chem. Commun.* **2025**, *61*, 12745–12748.
[52] Lu, T. A comprehensive electron wavefunction analysis toolbox for chemists, Multiwfn. *J. Chem. Phys.* **2024**, *161*, 082503.
[53] Lu, T.; Chen, F. W. Multiwfn: A multifunctional wavefunction analyzer. *J. Comput. Chem.* **2012**, *33*, 580–592.
[54] Wang, H. M.; Ma, B. Y.; Tian, J. L.; Niu, Z. Q. The design of chemically self-charging aqueous batteries. *Angew. Chem., Int. Ed.* **2025**, *64*, e202506922.
[55] An, L.; Zhao, T. S.; Yan, X. H.; Zhou, X. L.; Tan, P. The dual role of hydrogen peroxide in fuel cells. *Sci. Bull.* **2015**, *60*, 55–64.
[56] Yue, F.; Tie, Z. W.; Zhang, Y.; Bi, S. S.; Wang, Y. J.; Niu, Z. Q. Proton chemistry induced long-cycle air self-charging aqueous batteries. *Angew. Chem., Int. Ed.* **2022**, *61*, e202208513.
[57] Zhang, Y.; Wan, F.; Huang, S.; Wang, S.; Niu, Z. Q.; Chen, J. A chemically self-charging aqueous zinc-ion battery. *Nat. Commun.* **2020**, *11*, 2199.
[58] Zhong, L. H.; Wang, C. F.; He, J.; Lin, Z. Q.; Yang, X. D.; Li, R.; Zhan, S.; Zhao, L. W.; Wu, D.; Chen, H. et al. Self-charging aqueous Zn//COF battery with ultrahigh self-charging efficiency and rate. *Adv. Mater.* **2024**, *36*, 2314050.
[59] Kuchena, S.; Paudel, A.; Wu, Q. L.; Wang, Y. A novel aqueous zinc-ion battery capable of self-charging at low temperature. *J. Mater. Chem. A* **2024**, *12*, 2867–2876.